RSC Advances

PAPER

View Article Online
View Journal | View Issue

Cite this: *RSC Adv.*, 2024, **14**, 27412

Structural, morphological, magnetic and electrical properties of $La_{0.8}Na_{0.2-x}\square_xMnO_3$ ($0.00 \leq x \leq 0.15$) manganites†

M. Wali,[a] W. Hizi, *[b] R. Dhahri,[a] H. Rahmouni, [b] K. Khirouni[c] and E. Dhahri[a]

$La_{0.8}Na_{0.2-x}\square_xMnO_3$ ($0.00 \leq x \leq 0.15$) manganites were successfully synthesized using the solid-state route. X-ray diffraction was performed to check the samples' purity and phase structure. Scanning electron microscopy analysis reveals a decrease in the average grain size with an increase in the deficiency amount. Analysis of the temperature dependence of magnetization proved the presence of ferromagnetic–paramagnetic transition in all the studied samples. The magnetization derivative (d^2M/dT^2) curves demonstrated a decrease in the transition temperature with an increase in the deficiency amount. Such experimental observations can be correlated with bandwidth evolution, which affected double-exchange interactions. It can be equally accounted for by the average grain size decrease. In this regard, the experimental measurements of effective paramagnetic moments revealed the existence of ferromagnetic correlations within the paramagnetic phase. Notably, different electrical findings were addressed. Indeed, the frequency dependence of electrical conductivity displayed the coexistence of two frequency slopes reflecting the presence of Jonscher's double power law for all the studied samples. A significant decrease in conductivity values was observed when the deficiency amount increased. This experimental observation could be assigned to the decrease in the grain size (conductor region). Such assumption was confirmed by the evolution of the grain boundary resistance with deficiency level. Indeed, a significant mounting in the grain boundary resistance values was obtained presenting the increase of the resistive region for $x = 0.15$. It is worth noting that the Curie temperature for the $x = 0.10$ sample was found to be close to room temperature ($T_C = 297$ K). These findings make the $La_{0.8}Na_{0.1}\square_{0.1}MnO_3$ compound a powerful candidate for many technological applications.

Received 13th May 2024
Accepted 3rd August 2024

DOI: 10.1039/d4ra03519d

rsc.li/rsc-advances

1. Introduction

The discovery of the colossal magnetoresistance phenomenon[1–3] and magnetocaloric effect[4–6] has fueled much research on the outstanding physical properties of manganite compounds. Owing to such physical properties, manganites can be used for numerous applications, including magnetic refrigerants, magnetic sensors, magneto-resistive transducers, computer memory systems, spintronic devices, catalysts, and infrared detectors.[7–11] Different interesting behaviors such as charge-ordering (CO),[12] metamagnetic transition,[13] colossal magnetoresistance[14,15] and large magnetocaloric effects[6,16] have been observed. In fact, several studies have widely reported many investigations on the structural, morphological, optical, magnetic, electronic and electrical properties of manganites.[17–32] The parent compound ($LaMnO_3$) of lanthanum manganite ($La_{1-x}A_xMnO_3$) systems is an anti-ferromagnetic material.[33] Substitution by a monovalent (Na^+, Ag^+, K^+…) or divalent ion (Ca^{2+}, Sr^{2+}, Ba^{2+}…) generates mixed-valence properties. Indeed, the partial substitution of La element by Na element provokes the hopping of an e_g electron from the Mn^{3+} cation to the adjacent Mn^{4+} cation by the intermediary oxygen anion O^{2-}. Such hops manifest into double-exchange (DE) interactions between these manganese cations.[34] Accordingly, the Mn^{3+}/Mn^{4+} ratio can be controlled by doping (site of doping, doping element, doping amount), leading to an improvement in physical properties. In this context, the effect of sodium doping on lanthanum manganite systems has been frequently studied.[35–41] Arunachalam *et al.*[36] reported that the particle size decreases with increasing sodium concentration. Such structural change has an effect on the electrical and magnetic properties. In addition, the ferromagnetic–paramagnetic phase transition temperature is increased with the increasing Na concentration.[40] Furthermore, it was observed that the system resistivity values showed a significant decrease with

[a]*Laboratoire de Physique Appliquée, Faculté des Sciences de Sfax, Université de Sfax, B.P. 1171, 3000, Sfax, Tunisia*

[b]*Laboratoire de Recherche Matériaux Avancés et Nanotechnologies, Institut Supérieur des Sciences Appliquées et de Technologie de Kasserine, Université de Kairouan, BP 471, Kasserine 1200, Tunisia. E-mail: widedph@live.com*

[c]*Laboratoire de Physique des Matériaux et des Nanomatériaux appliquée à l'Environnement, Faculté des Sciences de Gabès cité Erriadh, Université de Gabès, 6079 Gabès, Tunisia*

† Electronic supplementary information (ESI) available. See DOI: https://doi.org/10.1039/d4ra03519d

the increase in the Na amount.[40] Besides, the literature[42–49] has presented that the creation of deficiencies can affect the physical properties of these kinds of systems. Indeed, A-site deficiency can modify the Mn^{3+}/Mn^{4+} amount, which in turn can alter their magnetic and electrical properties. A magnetocaloric effect (MCE) was also reported in several deficient manganites. Indeed, Smari *et al.*[50] argued that the $La_{0.5}Ca_{0.5-x}Ag_xMnO_3$ deficient manganite had a large ΔS_M^{max} of 2.9 J K^{-1} kg^{-1} under a magnetic field of 0.9 T with a T_C of 272 K. This indicates that $La_{0.5}Ca_{0.5-x}Ag_xMnO_3$ could be used as an active magnetic refrigerant within the sub-room-temperature range. In addition, M'nassri *et al.*[51] examined the effect of barium-deficiency on the structural, magnetic, and magnetocaloric properties of $La_{0.6}Sr_{0.2}Ba_{0.2-x}\square_xMnO_3$, where ΔS_M^{max} did not exceed 4 J K^{-1} kg^{-1} under a magnetic field of 4.5 T for all the studied samples.

In the present investigation, interesting properties of $La_{0.8}Na_{0.2-x}\square_xMnO_3$ ($0.00 \leq x \leq 0.15$) manganites were observed and discussed. The deficiency effect was obviously manifested in the structural, morphological, magnetic, and electrical properties. For instance, a decrease in the grain size was observed in the SEM study. The increasing deficiency level also provoked a decrease in the Curie temperature T_C. The experimental measurements of the effective paramagnetic moments exceeded the corresponding theoretical values. Such a result proved the existence of ferromagnetic correlations within the paramagnetic phase. On the electrical side, the presence of double slopes in the dispersive region of the conductivity spectra was revealed for all the studied samples, which equally displayed a significant decrease in the conductivity values when the deficiency amount rose. For $x = 0.10$, the Curie temperature was found to be close to room temperature ($T_C = 297$ K). Such an experimental observation makes the 10% deficiency sample a promising candidate for several technological applications.

2. Experimental details

The $La_{0.8}Na_{0.2-x}\square_xMnO_3$ ($0.00 \leq x \leq 0.15$) materials were synthesized *via* the solid-state ceramic technique. The used precursors were lanthanum La_2O_3 and manganese MnO_2 oxides as well as sodium carbonate Na_2CO_3 with purities greater than 99.9%. Lanthanum oxide and sodium carbonate were dehydrated at 400 °C for 1 h so as not to distort the weighing. The first synthesis step consisted of weighing the precursors in the desired stoichiometric proportions. These precursors were then finitely ground for 20 min to obtain a homogeneous mixture. The obtained powders were subsequently placed in alumina nacelles and brought to increasingly high temperatures, going from 700 °C to 1100 °C at an increase of 100 °C per day, interspersed with grinding. This step, called calcination, allowed, on the one hand the decomposition and release of gases (O_2 and CO_2) and, on the other hand, the partial formation of the intended phase in line with the following reaction:

$$0.4La_2O_3 + \left(\frac{0.2-x}{2}\right)Na_2CO_3 + MnO_2 \rightarrow La_{0.8}Na_{0.2-x}\square_xMnO_3 + \delta CO_2 + \mu O_2 \quad (1)$$

The obtained powders were ground again for 30 min in a dry environment. This grinding reduced the grain size, homogenized the product, and minimized the intergranular porosity. The next step consisted of pelletizing the samples to promote diffusion and vaporization–condensation mechanisms during the solid-state reaction. During this phase, the powders were molded into pellets under an axial pressure of 4 tons per cm^2. The final step was sintering, which consisted of placing the pellets, in alumina or platinum crucibles to guarantee that a foreign phase was not formed by interaction with the crucible, in an oven under air at 1200 °C for an annealing time sufficient for the formation and growth of and grains. Rapid quenching in air was necessary to help maintain the structure at ambient temperature in equilibrium with the annealing temperature. These reactions are slow and result in a long-distance diffusion of the different ions. These methods have the advantage of being very easy to implement; however, they require several grinding and annealing cycles at high temperatures.

Alternatively, the samples underwent X-ray diffraction analysis using a Bruker D8 diffractometer, which featured a copper anticathode ($\lambda_{Cu\alpha1} = 1.5406$ Å) and a rear graphite monochromator. The recording of the X-ray powder patterns was carried out at room temperature in an angular range varying from 10° to 100° in the 2θ mode at steps of 0.02° and an acquisition time of 1 s for each step.

The microstructure was examined by scanning electron microscopy (SEM). A vibrating sample magnetometry (VSM) instrument by Quantum Design was employed for the measurements of the magnetic fields. The magnetization *versus* magnetic field curves were recorded by varying the magnetic field between 0 and 5 T at temperatures both below and above the Curie temperature.

Electrical measurements were performed using an Agilent 4294A impedance analyzer for each prepared sample over a wide frequency range (40 Hz to 1 MHz) at room temperature.

3. Results and discussion

3.1. Scanning electron microscopy

The secondary electron SEM images for $La_{0.8}Na_{0.2-x}\square_xMnO_3$ ($0.00 \leq x \leq 0.15$) are shown in Fig. 1(a)–(d). The micrographs obtained showed grains with various polygonal shapes with a non-uniform distribution. We could also observe in these images some black contrast voids associated with the porosity of the samples. The particle-size distribution was analyzed statistically using ImageJ software. Fig. 2(a)–(d) depicts histograms illustrating the grain sizes of the samples under investigation. As observed, the histograms were well modeled by the Lorentzian function. The average grain size was affected by the sodium vacancy rate, resulting in different values for the four samples: 2.358 μm for $x = 0.00$, 2.292 μm for $x = 0.05$, 2.087 μm for $x = 0.10$, and 1.994 μm for $x = 0.15$.

3.2. Chemical analysis

The percentages of Mn^{3+} and Mn^{4+} ions in our $La_{0.8}{}^{3+}Na_{0.2-x}{}^{+}\square_x{}^{0}(Mn_{0.6-x}{}^{3+}Mn_{0.4+x}{}^{4+})O_3{}^{2-}$ samples were

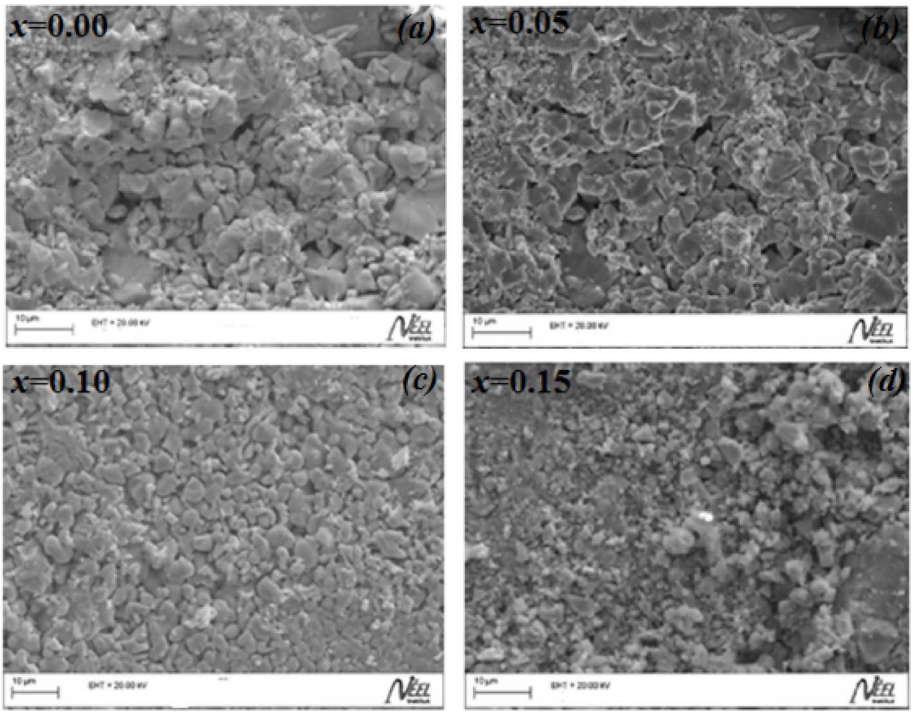

Fig. 1 SEM images of all samples: (a) $x = 0.00$, (b) $x = 0.05$, (c) $x = 0.10$ and (d) $x = 0.15$.

determined using a conventional chemical technique. Initially, we dissolved the sample powder in oxalic acid dihydrate ($H_2C_2O_4 \cdot 2H_2O$) and concentrated sulfuric acid (H_2SO_4). The resulting solutions were subsequently titrated with potassium permanganate ($KMnO_4$). Table 1 depicts a comparison of the theoretical and experimental results of the Mn^{3+} and Mn^{4+} contents. The obtained data indicate that the experimental concentrations of manganese ions were very close to the theoretical values. Ultimately, it is noteworthy that our samples were prepared in air, ensuring they were stoichiometric in oxygen.

3.3. Structural properties

The X-ray diffraction pattern analysis confirmed the structural integrity and phase purity of our compounds. The X-ray diffraction patterns at room temperature for the $La_{0.8}Na_{0.2-x}\square_xMnO_3$ ($0.00 \leq x \leq 0.15$) compounds are depicted in Fig. 3(a), which indicate that all the samples exhibited a consistent perovskite structure with identical peaks. These peaks were associated with the diffraction lines of the rhombohedral phase with the $R\bar{3}c$ space group. All the peaks accurately correlated with the 2θ values of 23.3°, 32.4°, 33.2°, 40.1°,40.8° 47°, 59°, 69.4°, and 77.9° indicating the 012, 110, 104, 113, 202, 024, 214, 220, and 134 crystalline planes, respectively.

Also, with the increase in vacancy content, the patterns showed a slight shift of the most intense peak toward smaller 2θ values (inset of Fig. 3(a)), suggesting that the vacancy had a larger ionic radius than Na. The displacement of the diffraction peaks toward smaller angles indicated that the cell parameters of the samples increased as the vacancy rate increased. The Rietveld technique produced satisfactory agreement factors and lattice parameters when refining the data using FULLPROF software.[52] An example of the XRD pattern refinement for the $x = 0.15$ sample is shown in Fig. 3 (b). The refinement results (see the ESI†), as summarized in Table 2, indicated there was a slight increase in both the cell parameter and unit cell volume with the rising vacancy content.

In fact, we noted the existence of very low intensity peaks in the XRD patterns, which were associated with Mn_3O_4, as is frequently encountered in mixed-valence manganites. This Mn_3O_4 secondary phase had no significant effect on the stoichiometry of the materials, given its low concentration.[53] Furthermore, it is important to highlight that the introduction of sodium vacancies did not lead to any changes in the space group of the parent compound $La_{0.8}Na_{0.2}MnO_3$. The average crystallite size has been estimated using a variety of techniques, such as Scherrer's formula.[54,55] The following formula was utilized here to calculate the average crystallite size D_{SC}:

$$D_{SC} = \frac{0.9\lambda}{\beta \cos \theta} \quad (2)$$

This formula makes it possible to extract the microstructural parameters of the diffraction peaks, but it only gives partial information. In this relationship, the broadening of the line characterized by the width at half maximum is linked to an effect of the size of the coherent diffraction domains (crystallite size). Applying Scherrer's formula, we calculated the size of the crystallites within our compounds, observing an increase as the vacancy rate (x) increased. The respective values for the four samples ($x = 0.00$, $x = 0.05$, $x = 0.10$, and $x = 0.15$) were 95,

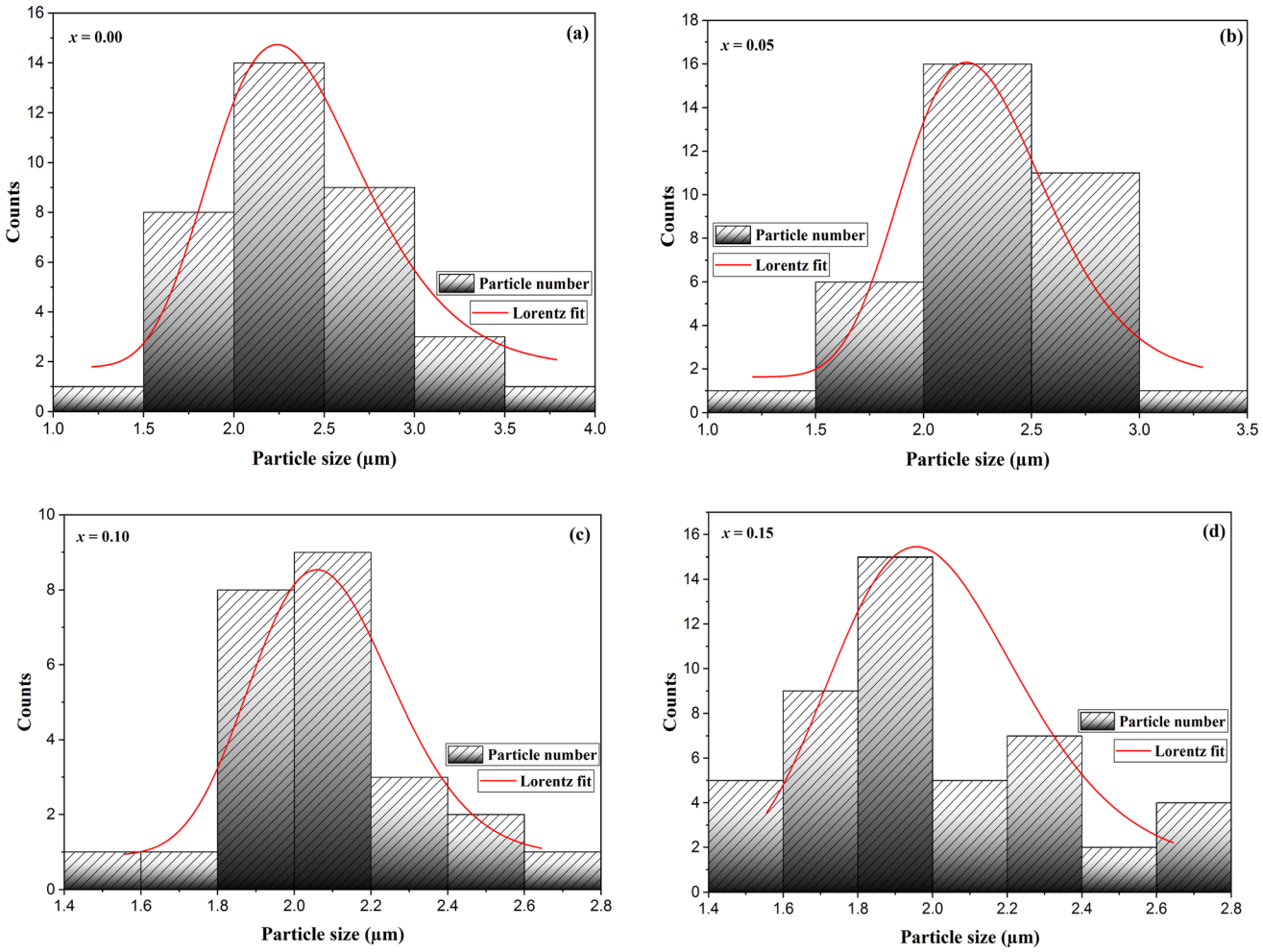

Fig. 2 Size-distribution histograms of $La_{0.8}Na_{0.2-x}\square_xMnO_3$: (a) $x = 0.00$, (b) $x = 0.05$, (c) $x = 0.10$ and (d) $x = 0.15$.

Table 1 Chemical analysis results for $La_{0.8}Na_{0.2-x}\square_xMnO_3$ samples with $0.00 \leq x \leq 0.15$

	Theoretical content		Experimental content	
x	Mn^{3+} (%)	Mn^{4+} (%)	Mn^{3+} (%)	Mn^{4+} (%)
0.00	60	40	62.14	37.86
0.05	55	45	56.02	43.98
0.10	50	50	51.17	48.83
0.15	45	55	45.84	54.16

108.2, 108.5, and 109.5 nm. The elemental volume increased as the vacancy rate rose, shifting from 55.5 Å to 56.5 Å when the vacancy rate increased from 0.00 to 0.15. To elucidate this variation, we took into account the following three factors:

- Variation in the average radius of B sites,
- Variation in the average radius of A sites,
- Variation of the Mn–O distance.

According to electrical neutrality, the $La_{0.8}{}^{3+}Na_{0.2-x}{}^{+}\square_x{}^{0}(Mn_{0.6-x}{}^{3+}Mn_{0.4+x}{}^{4+})O_3{}^{2-}$ compounds contain $(0.6 - x)$ Mn^{3+} ions and $(0.4 + x)$ Mn^{4+} ions per formula unit. By increasing the rate of vacancies x, there is a conversion of a fraction x of the manganese Mn^{3+} ions into Mn^{4+} ions, whose radius is smaller ($r_{Mn^{3+}} = 0.65$ Å and $r_{Mn^{4+}} = 0.53$ Å[56]). Thus, the average ionic radius $\langle r_B \rangle$ of the cations occupying the B site was determined from the following relation:

$$\langle r_B \rangle = (0.6 - x)r_{Mn^{3+}} + (0.4 + x)r_{Mn^{4+}} \quad (3)$$

We observed that the variation in the average radius $\langle r_B \rangle$ of the cations at the B site decreased, unlike the volume V, which increased with the vacancy rate x. This reduction in $\langle r_B \rangle$ did not significantly affect the volume variation, as it did not exceed ~2% in the best cases. To explain this evolution in volume, we studied the effect of a second parameter, namely the average ionic radius $\langle r_A \rangle$ of the cations occupying the A site. Thus, the creation of vacancies at the sodium site in the $La_{0.8}Na_{0.2-x}\square_xMnO_3$ series could increase the average ionic radius of the A site (with $r_{La^{3+}} = 1.216$ Å and $r_{Na^{+}} = 1.24$ Å); therefore $r_V > r_{Na^{+}}$. The creation of a vacancy in a monovalent or divalent site tends to increase the volume in relation to the vacancy rate x.[57] Khlifi *et al.*[57] showed, in the $La_{0.8}Ca_{0.2-x}\square_xMnO_3$ series, that the vacancy would admit an r_V radius greater than that of calcium ($r_{Ca^{2+}} = 1.18$ Å), consequently resulting in an expansion of the

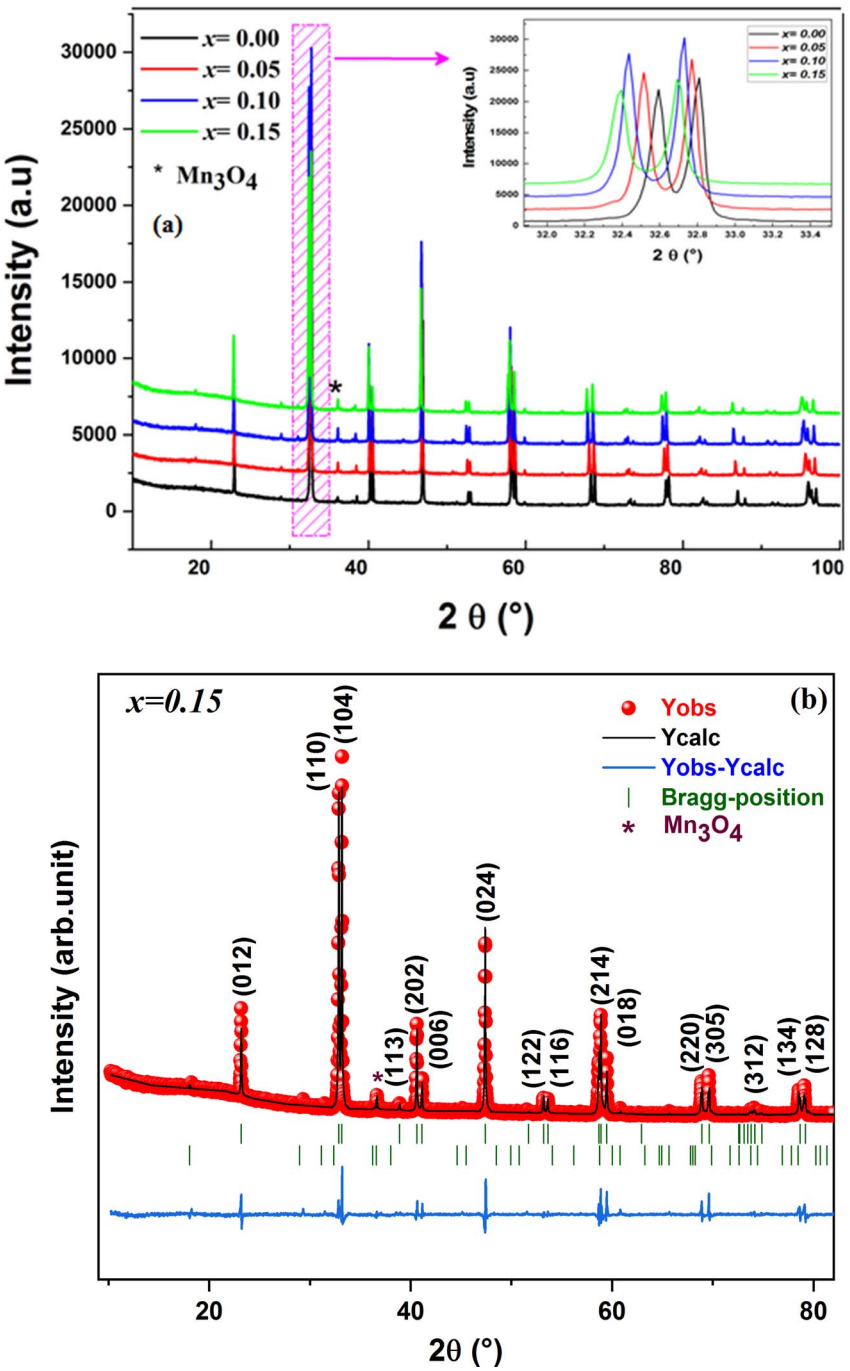

Fig. 3 XRD patterns of $La_{0.8}Na_{0.2-x}\square_xMnO_3$ compounds. The peaks were indexed to the $R\bar{3}c$ space group. The inset displays a deviation of the peaks toward lower angles for the most intense peaks (Bragg reflections 110 and 104) (a). Experimental XRD diagram and Rietveld refinement for $La_{0.8}Na_{0.05}\square_{0.15}MnO_3$ (b).

unit cell volume. Whereas the formation of a vacancy in a trivalent site typically results in a reduction in volume.[58] Likewise, Skini *et al.*[58] showed that, in $La_{0.8-x}\square_xCa_{0.2}MnO_3$ compounds, the radius of the vacancy r_V was smaller than $r_{La^{3+}}$ = 1.216 Å. Then, $r_{Ca^{2+}} \leq r_V \leq r_{La^{3+}}$, causing a decrease in volume.

According to the structural refinement, we noticed that the Mn–O distance increased from 1.9250 Å to 1.9404 Å when the rate of vacancies in the A sites passed from 0.00 to 0.15. This variation in the Mn–O distance directly affected the cell parameters, which increased, and consequently the volume of the cell increased with the rate of vacancies in A sites increasing. In Fig. 4, we plotted the changes in both the Mn–O distance and the volume against the vacancy rate x. This graph vividly demonstrates there was an upward trend in the Mn–O distance, providing a clear explanation for the concurrent increase in volume as the vacancy rate x rose.

Table 2 Refinement results for the XRD experimental patterns

Vacancy content	x		0.00	0.05	0.10	0.15
$La_{0.8}Na_{0.2-x}\square_xMnO_3$ (rhombohedral), $R\bar{3}c$	Lattice parameters	$a = b$ (Å)	5.412(6)	5.427(5)	5.440(1)	5.448(7)
		c (Å)	13.132(4)	13.145(3)	13.153(2)	13.16(5)
	Unit cell volume (Å^3)		55.531	55.892	56.185	56.415
	d_{Mn-O} (Å)		1.9250	1.9336	1.9374	1.9404
	$\theta_{Mn-O-Mn}$ (°)		164.5877	162.7587	162.5934	162.4338
	R_{wp} (%)		5.20	5.36	6.14	4.68
	R_p (%)		5.04	4.68	5.02	4.49
	R_f (%)		2.18	2.24	1.18	1.81
	χ^2 (%)		3.41	4.13	2.74	2.11
Mn_3O_4 (tetragonal), $I4_1/amd$	Lattice parameters	$a = b$ (Å)	5.734(6)	5.731(8)	5.731(5)	5.739(4)
		c (Å)	9.467(9)	9.458(7)	9.453(5)	9.455(2)
	%		0.08	0.11	0.08	0.16

3.4. Magnetic properties

The magnetic properties were investigated by measuring the temperature-dependent magnetization ($M(T)$) under an applied field of 0.05 T for the compounds $La_{0.8}Na_{0.2-x}\square_xMnO_3$ with vacancy rates ranging from 0.00 to 0.15, as illustrated in Fig. 5(a)–(d). The findings revealed a transition from ferromagnetic to paramagnetic states for all the samples as the temperature increased.[59] Accordingly, it was evident that the magnetization declined as the sodium deficiency rate increased, attributable to the diminished presence of Mn^{3+} ions, distinguished by their elevated spin ($S = 2$), and the concomitant augmentation of Mn^{4+} ions ($S = 3/2$), as delineated by the equation $La_{0.8}{}^{3+}Na_{0.2-x}{}^{+}\square_x{}^{0}(Mn_{0.6-x}{}^{3+}Mn_{0.4+x}{}^{4+})O_3{}^{2-}$. Furthermore, there are two techniques available to identify the transition temperature (T_C) from the ferromagnetic to the paramagnetic state.

Method I. Through numerical derivation (d^2M/dT^2), as shown in the insets of Fig. 5(a)–(d), whereby it is possible to precisely identify the transition's inflection point.

Method II. By determining the saturation magnetization and the Curie temperature T_C using the following equation as presented in Fig. 5(a)–(d):

$$M(T) = M_{Sat}\frac{\left(1-\frac{T}{T_C}\right)^{\varepsilon}}{1-\varepsilon\left(\frac{T}{T_C}\right)+\sigma\left(\frac{T}{T_C}\right)^{\frac{3}{2}}-\delta\left(\frac{T}{T_C}\right)^{\frac{7}{2}}} \quad (4)$$

where ε, δ, and σ are constant parameters. The adjusted parameters obtained from the refinement of the magnetization as a function of temperature curve are illustrated in Table 3. The Curie temperature (T_C) delineating the transition between the paramagnetic and ferromagnetic phases exhibited a decrease from 336 K to 263 K as the sodium deficiency (x) increased from 0.00 to 0.15. These findings were in excellent accordance with those reported by Wali *et al.*[59] The reduction in T_C could be ascribed to several factors, notably a direct correlation with the bandwidth (W), which affects both the mobility of e_g electrons and the double-exchange (DE) interaction. Indeed, the

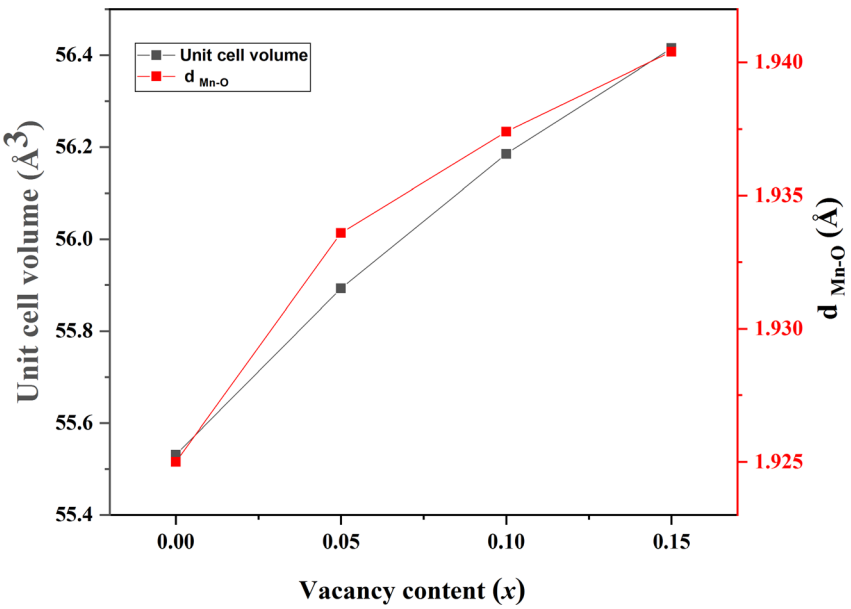

Fig. 4 Variation in the volume V and the distance d_{Mn-O} as a function of the x rate vacancy of $La_{0.8}Na_{0.2-x}\square_xMnO_3$ compounds ($x = 0.00$, 0.05, 0.10 and 0.15).

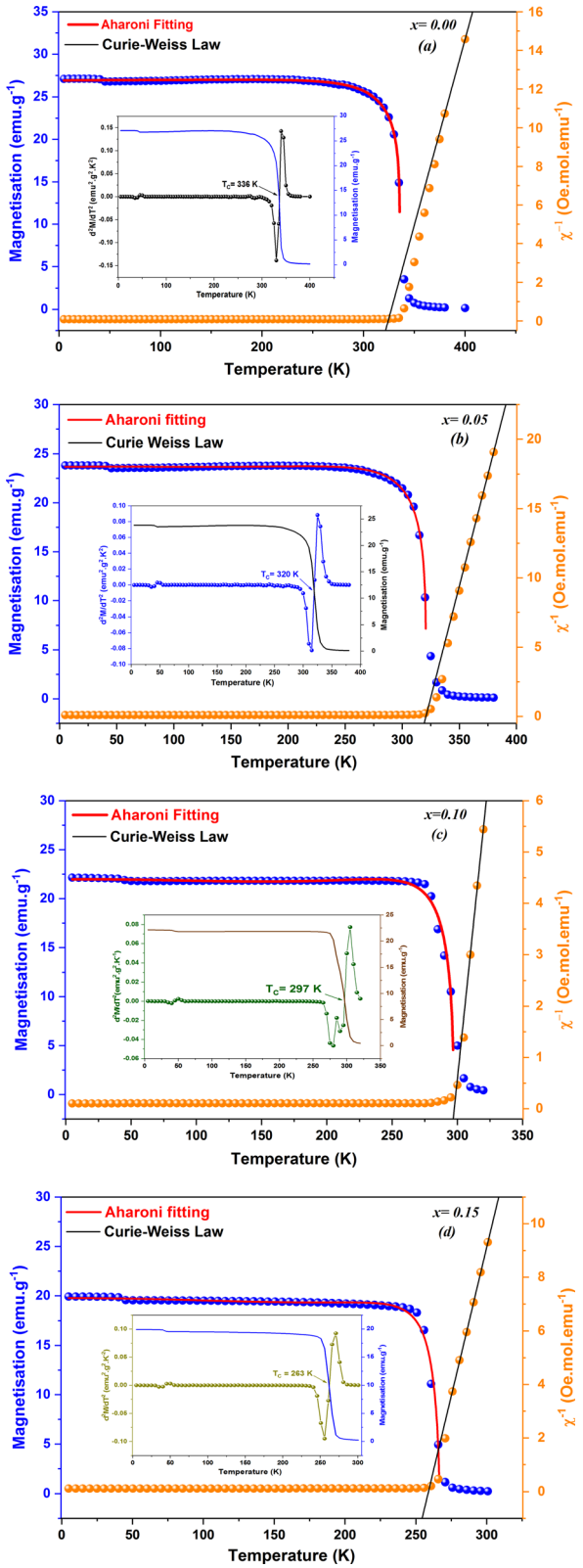

Fig. 5 Variation in the magnetization (M) and the inverse of the magnetic susceptibility *vs.* temperature of $La_{0.8}Na_{0.2-x}\square_xMnO_3$ (x = 0.00 (a), 0.05 (b), 0.10 (c) and 0.15 (d)) compounds measured at an applied magnetic field of 0.05 T. Symbols are the experimental results and solid lines are the graphs fitted. The insets display the numerical derivation d^2M/dT^2 as a function of temperature for all the samples.

Table 3 Aharoni fitting parameters

x	M_{Sat} (emu g^{-1})	T_C^{theo} (K)	T_C^{exp} (K)
0.00	26.91	335.65	336
0.05	23.67	320.68	320
0.10	21.97	296.98	297
0.15	19.76	266.61	263

introduction of a sodium vacancy in site A initiates a partial transformation of Mn^{3+} ions into Mn^{4+} ions, in accordance with the electronic formula $La_{0.8}{}^{3+}Na_{0.2-x}{}^{+}\square_x{}^{0}(Mn_{0.6-x}{}^{3+}Mn_{0.4+x}{}^{4+})O_3{}^{2-}$. As the vacancy rate escalated from 0.00 to 0.15, the number of tetravalent Mn^{4+} ions increased from 40% to 55%, while the number of trivalent Mn^{3+} ions decreased from 60% to 45%. This shift in the Mn^{3+}/Mn^{4+} ratio led to a reduction in the average ionic radius of the B site. Furthermore, owing to electrostatic reasons, a vacancy possesses a non-zero radius, further modifying the average ionic radius of the A site. These dual effects explain the decrease in magnetization and the Curie temperature (T_C) as the vacancy rate increased. Additionally, this alteration in the Mn^{3+}/Mn^{4+} ratio associated with sodium vacancies promoted an increase in the super-exchange interactions, thereby enhancing double exchange. It is evident that the magnetic properties of manganites are closely tied to the lengths and angles of the Mn–O–Mn bonds. The strength of the exchange interactions relies on both the bond distance and the bond angle. Consequently, reducing the angle and increasing the bond length weaken the Mn–Mn exchange interaction, resulting in a decrease in the Curie temperature (T_C) and magnetization.

Moreover, to understand the magnetic behavior within the paramagnetic range, we investigated the temperature dependence of the inverse magnetic susceptibility (χ) for all the samples, as depicted in Fig. 5(a)–(d). It is evident that the $1/\chi$ dependence of the temperature follows the Curie–Weiss law: $\chi = \frac{C}{T-\theta_W}$, where the Curie constant and Weiss temperature are represented by C and θ_W, respectively. The data's linear paramagnetic region can be used to obtain the Curie–Weiss parameters C and θ_W. Moreover, we calculated the experimental effective moment (μ_{eff}^{exp}), which is defined as: $\mu_{eff} = \sqrt{\frac{3K_B}{N\mu_B}}C$,[60] where N is the Avogadro number, μ_B is the Bohr magneton, and k_B is the Boltzmann constant. We found the μ_{eff}^{exp} values were 5.634, 4.775, 5.203, and 5.830 respectively. Assuming the orbital contribution to be quenched in both Mn^{3+} and Mn^{4+}, the theoretical paramagnetic effective moment (μ_{eff}^{th}) can be expressed as $g\sqrt{S(S+1)}\,\mu_B$, where $g = 2$ represents the gyromagnetic factor and S is the spin of the cation. Therefore, the theoretical values were $\mu_{eff}^{th} = 4.90\ \mu_B$ for Mn^{3+} and $\mu_{eff}^{th} = 3.87\ \mu_B$ for Mn^{4+}. Taking into account the rigid coupling of Mn^{3+} and Mn^{4+}, the calculated effective paramagnetic moment per formula unit can be written as:

$$\mu_{\text{eff}}^{\text{th}} = \sqrt{(0.6 - x)\left[\mu_{\text{eff}}^{\text{th}}(\text{Mn}^{3+})\right]^2 + (0.4 + x)\left[\mu_{\text{eff}}^{\text{th}}(\text{Mn}^{4+})\right]^2}\ \mu_{\text{B}} \quad (5)$$

The theoretical values of the effective paramagnetic moments $\mu_{\text{eff}}^{\text{th}}$ were calculated for all samples as 4.516, 4.465, 4.415, and 4.363 μ_{B} for $x = 0.00$, 0.05, 0.10, and 0.15, respectively. However, the experimental measurements of the effective paramagnetic moments surpassed the corresponding theoretical values. This discrepancy indicated the presence of Mn^{4+} and Mn^{3+} clusters,[61] suggesting that in the paramagnetic state, the individual magnetic spins were not isolated; instead, they formed small groups, revealing the existence of ferromagnetic correlations within the paramagnetic phase. In Table 4, we report the Curie constant (C), the Weiss temperature (θ_{W}), as well as the theoretical ($\mu_{\text{eff}}^{\text{th}}$) and experimental ($\mu_{\text{eff}}^{\text{exp}}$) moments. In the table, positive values of θ_{W} could be observed, confirming the ferromagnetic characteristics of all the samples. Additionally, these values exhibited a decreasing trend with increasing x, mirroring the behavior of the Curie temperature (T_{C}).

3.5. Electrical properties

Fig. 6 shows the electrical AC-conductivity spectrum for the parent compound $La_{0.8}Na_{0.2}MnO_3$. A frequency-independent region could be clearly observed at low frequencies. Such a frequency range is associated with the DC-conductivity, as depicted in Fig. 6. Funke[62] explained the electrical transport in such a regime by the long-range translational motion. Here, σ_{AC} remained constant as the frequency increased until reaching the hopping frequency. Such a characteristic frequency is defined by the frequency at which the conductivity changes the slope. Beyond this frequency, the electrical conductivity increased with the frequency increasing. Such an observation suggests the possibility of the presence of different electrical transport mechanisms, which has been widely studied using the Pike model[63] and detected in several amorphous and perovskite materials.[17–20,26,27,29,64–70] As indicated in Fig. 6, σ_{AC} showed a significant increase with two linear slopes. Thus, such a result leads to the fact that this spectrum presented two frequency exponents. Accordingly, the frequency dependence of AC-conductivity was governed by Jonscher's double power law:[71–73]

$$\sigma_{\text{AC}} = \sigma_{\text{DC}} + A_1\omega^{s_1} + A_2\omega^{s_2} \quad (6)$$

Table 4 Transition temperature (T_{C}), Curie constant (C), Curie–Weiss temperature (θ_{W}), theoretical ($\mu_{\text{eff}}^{\text{th}}$) and experimental ($\mu_{\text{eff}}^{\text{exp}}$) moments as a function of the x content for $La_{0.8}Na_{0.2-x}\square_xMnO_3$ samples

x	T_{C} (K)	C (K uem mol^{-1})	θ_{W} (K)	$\mu_{\text{eff}}^{\text{th}}$ (μ_{B})	$\mu_{\text{eff}}^{\text{exp}}$ (μ_{B})
0.00	336	3.968	338.024	4.516	5.634
0.05	320	2.850	323.888	4.465	4.775
0.10	297	3.384	300.159	4.415	5.203
0.15	263	4.248	260.064	4.363	5.830

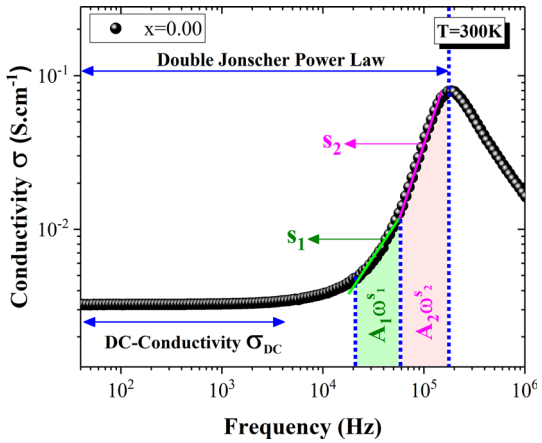

Fig. 6 Frequency dependence of electrical conductivity at room temperature for the parent compound $La_{0.8}Na_{0.2}MnO_3$.

where σ_{DC} is the DC-conductivity, A_1 and A_2 are constants, s_1 and s_2 are the frequency exponents, and $A_1\omega^{s_1}$ and $A_2\omega^{s_2}$ are the intermediate- and high-frequency responses of the AC-conductivity σ_{AC}, respectively. Such a result was detected for

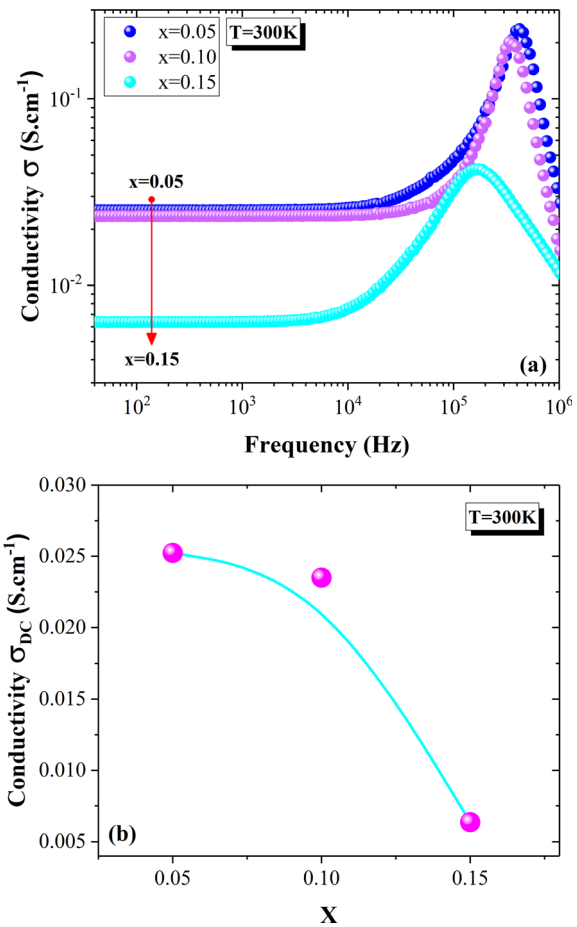

Fig. 7 Conductivity spectra of $La_{0.8}Na_{0.2-x}\square_xMnO_3$ (x = 0.05, 0.10 and 0.15) compounds (a). Evolution of DC-conductivity with the deficiency amount (b).

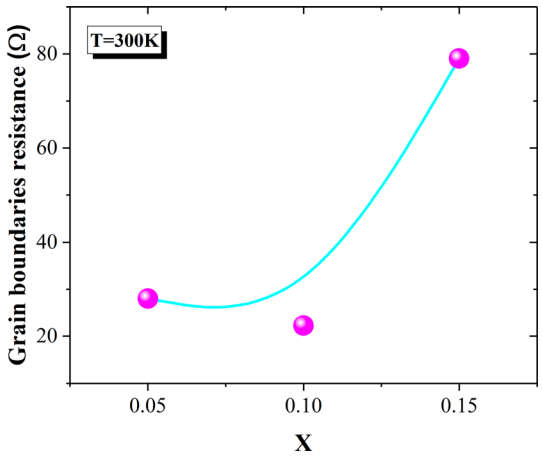

Fig. 8 Evolution of the grain boundary resistance with the deficiency amount.

all the studied samples (Fig. 7(a)). In fact, the frequency increase led to an increase in the crystal vibration, which contributed to releasing the trapped charge carriers. Equally, it can create new conduction sites. In this case, the inter-sites distance was decreased, presenting a short-range translational motion at intermediate and high frequencies.

The conductivity spectra of the $La_{0.8}Na_{0.2-x}\square_xMnO_3$ ($x = 0.05$, 0.10, 0.15) compounds are displayed in Fig. 7(a). At low frequencies, the conductivity showed a slight decrease with the deficiency ratio increasing from $x = 0.05$ to $x = 0.10$ (Fig. 7(a) and (b)). Then, a significant decrease in the conductivity values was observed when the deficiency ratio increased for $x = 0.15$. Various studies have reported that the transport properties in manganites are mainly controlled by the Mn^{3+}–O^{2-}–Mn^{4+} network and thus the Mn^{3+}/Mn^{4+} concentration.[17–19] Such a concentration can be modified by the bond length Mn–O, the bond angle Mn–O–Mn, the unit cell volume, the average grain size, and the oxygen vacancies.[17–20,26,74] In our case, the decrease in the conductivity values could be explained by the decrease in the grain size (Fig. 1(a)–(d)), which prevented the double-exchange interactions. Indeed, the SEM micrographs showed a decrease in the average grain size with increasing the deficiency rate (2.358, 2.292, 2.087, and 1.994 μm respectively for $x = 0.00$, 0.05, 0.10, and 0.15) (Fig. 1(a)–(d)). In the literature,[17,29,75–79] it has been frequently proved in manganites that the grain boundaries are more resistive than the grains. This could be due to the non-stoichiometric distribution of oxygen and the existence of dangling bonds in the grain boundaries region.[80] These factors can lead to charge trapping and an increase in the barrier width, which would hamper the DE interactions in the Mn^{3+}–O^{2-}–Mn^{4+} chain. Therefore, the decrease in the conductor region (grains) leads then to an increase in the resistive region (grain boundaries) and the reduction of the grains connectivity when the deficiency ratio increases. Fig. 8 confirmed the significant increase in the grain boundary resistance for $x = 0.15$; whereas, such resistance values were very close for $x = 0.05$ and $x = 0.10$. Thus, the electrical conductivity decrease was an expected result (Fig. 7(a) and (b)).

4. Conclusion

Deficient $La_{0.8}Na_{0.2-x}\square_xMnO_3$ ($x = 0.00$, 0.05, 0.10, and 0.15) manganites were successfully prepared *via* a solid-state reaction. The phase formation of the synthesized samples was confirmed using X-ray diffraction diagrams. The scanning electron microscopy analysis revealed there was a decrease in the average grain size. The evolution of magnetization (measured under an applied field of 0.05 T) with temperature indicated the presence of a ferromagnetic–paramagnetic transition for all the compounds. The transition temperature T_C was found to decrease when the deficiency ratio increased. Measurements of the effective paramagnetic moments revealed the existence of ferromagnetic correlations within the paramagnetic phase. However, the electrical conductivity spectra showed the coexistence of two frequency slopes mirroring the presence of Jonscher's double power law. As the deficiency amount increased, a significant decrease in the conductivity values was obviously detected. Such an experimental result could be related to the decrease in the grain size. The significant increase in the grain boundary resistance for $x = 0.15$ confirmed the grain size effect on the transport properties. Eventually, it was observed that the Curie temperature for $x = 0.10$ was close to room temperature ($T_C = 297$ K). Such a result indicates that the 10% deficiency sample may be a promising candidate for several technological applications.

Ethical approval

This article does not contain any studies involving animal or human participants performed by any of the authors.

Data availability

The data included in this manuscript are available and can be discussed (or shared), on request from the corresponding author.

Author contributions

All the authors have accepted full responsibility for the content of this manuscript and have given their approval to its submission.

Conflicts of interest

There are no conflicts to declare.

Acknowledgements

This study is supported by the Tunisian Ministry of Higher Education and Scientific Research.

References

1 R. von Helmolt, J. Wecker, B. Holzapfel, L. Schultz and K. Samwer, Giant negative magnetoresistance in perovskite

like $La_{2/3}Ba_{1/3}MnO_x$ ferromagnetic films, *Phys. Rev. Lett.*, 1993, **71**, 2331.
2 S. Jin, T. H. Tiefel, M. McCormack, R. A. Fastnacht, R. Ramesh and L. H. Chen, Thousandfold change in resistivity in magnetoresistive La-Ca-Mn-O films, *Science*, 1994, **264**, 413.
3 M. McCormack, S. Jin, T. H. Tiefel, R. M. Fleming, J. M. Phillips and R. Ramesh, Very large magnetoresistance in perovskite-like La-Ca-Mn-O thin films, *Appl. Phys. Lett.*, 1994, **64**, 3045.
4 R. D. McMichael, R. D. Shull, L. J. Swartzendruber, L. H. Bennett and R. E. Watson, Magnetocaloric effect in superparamagnets, *J. Magn. Magn. Mater.*, 1992, **111**, 33.
5 V. K. Pecharsky and K. A. Gschneidner Jr, Magnetocaloric effect and magnetic refrigeration, *J. Magn. Magn. Mater.*, 1999, **200**, 44.
6 V. Franco, J. S. Blázquez, J. J. Ipus, J. Y. Law, L. M. Moreno-Ramírez and A. Conde, Magnetocaloric effect: From materials research to refrigeration devices, *Prog. Mater. Sci.*, 2018, **93**, 112.
7 S. Saha, K. Das, S. Bandyopadhyay and I. Das, A-site cationic disorder induced significantly large magnetoresistance in polycrystalline $La_{0.2}Gd_{0.5}Ba_{0.3}MnO_3$ compound, *J. Magn. Magn. Mater.*, 2017, **442**, 196.
8 Z. C. Xia, S. L. Yuan, W. Feng, L. J. Zhang, G. H. Zang, J. Tang, L. Liu, D. W. Liu, Q. H. Zheng, L. Chen, Z. H. Fang, S. Liu and C. Q. Tang, Magnetoresistance and transport properties of different impurity doped $La_{0.67}Ca_{0.33}MnO_3$ composite, *Solid State Commun.*, 2003, **127**, 567.
9 Q. Zhang, L. Yin, W. Mi and X. Wang, Large Spatial Spin Polarization at Benzene/$La_{2/3}Sr_{1/3}MnO_3$ Spinterface: Toward Organic Spintronic Devices, *J. Phys. Chem. C*, 2016, **120**, 6156.
10 D. Robinson, C. Sepúlveda, E. J. Delgado, O. Peña, J. L. G. Fierro and G. Pecchi, Electronic properties and catalytic performance for DME combustion of lanthanum manganites with partial B-site substitution, *J. Catal.*, 2016, **338**, 47.
11 N. Khare, D. P. Singh, H. K. Gupta, P. K. Siwach and O. N. Srivastava, Preparation and study of silver added $La_{0.67}Ca_{0.33}MnO_3$ film, *J. Phys. Chem. Solids*, 2004, **65**, 867.
12 Y. Tokura, *Colossal Magnetoresistive Oxides*, Gordon and Breach Science, New York, 2000.
13 T. Elovaara, H. Huhtinen, S. Majumdar and P. Paturi, Irreversible metamagnetic transition and magnetic memory in small-bandwidth manganite $Pr_{1-x}Ca_xMnO_3$ (x = 0.0–0.5), *J. Phys.: Condens. Matter*, 2012, **24**, 216002.
14 Y. Tokura, Critical features of colossal magnetoresistive manganites, *Rep. Prog. Phys.*, 2006, **69**, 797.
15 A.-M. Haghiri-Gosnet and J.-P. Renard, CMR manganites: physics, thin films and devices, *J. Phys. D: Appl. Phys.*, 2003, **36**, R127.
16 V. S. Kolat, T. Izgi, A. O. Kaya, N. Bayri, H. Gencer and S. Atalay, Metamagnetic transition and magnetocaloric effect in charge-ordered $Pr_{0.68}Ca_{0.32-x}Sr_xMnO_3$ (x = 0, 0.1, 0.18, 0.26 and 0.32) compounds, *J. Magn. Magn. Mater.*, 2010, **322**, 427.
17 H. Rahmouni, M. Smari, B. Cherif, E. Dhahri and K. Khirouni, Conduction mechanism, impedance spectroscopic investigation and dielectric behavior of $La_{0.5}Ca_{0.5-x}Ag_xMnO_3$ manganites with compositions below the concentration limit of silver solubility in perovskites ($0 \leq x \leq 0.2$), *Dalton Trans.*, 2015, **44**, 10457.
18 B. Cherif, H. Rahmouni, M. Smari, E. Dhahri, N. Moutia and K. Khirouni, Transport properties of silver–calcium doped lanthanum manganite, *Phys. B*, 2015, **457**, 240.
19 W. Hizi, H. Rahmouni, K. Khirouni and E. Dhahri, Investigation of charge-carriers dynamics and sub/super-linear response for $La_{0.8}Na_{0.2-x}\square_xMnO_3$ (x = 0 and 0.1) perovskite ceramics, *Phys. B*, 2024, **673**, 415423.
20 W. Hizi, H. Rahmouni, K. Khirouni and E. Dhahri, Nanoparticles size effect on transport properties of doped manganite elaborated by sol–gel route, *J. Mater. Sci.: Mater. Electron.*, 2023, **34**, 1173.
21 H.-Y. Hou, S. Tian, H.-R. Ge, J.-D. Chen, Y.-Q. Li and J.-X. Tang, Recent progress of polarization-sensitive perovskite photodetectors, *Adv. Funct. Mater.*, 2022, **32**, 2209324.
22 S. Othmani, R. Blel, M. Bejar, M. Sajieddine, E. Dhahri and E. K. Hlil, New complex magnetic materials for an application in Ericsson refrigerator, *Solid State Commun.*, 2009, **149**, 969.
23 A. Žužić, L. Pavić, A. Bafti, S. Marijan, J. Macan and A. Gajović, The role of the A-site cation and crystal structure on the electrical conductivity of strontium-doped calcium and barium manganites, *J. Alloys Compd.*, 2023, **935**, 167949.
24 D. I. Pchelina, V. D. Sedykh, N. I. Chistyakova, V. S. Rusakov, Y. A. Alekhina, A. N. Tselebrovskiy, B. Fraisse, L. Stievano and M. T. Sougrati, The structural and magnetic features of perovskite oxides $La_{1-x}Sr_xMnO_{3+\delta}$ (x = 0.05, 0.10, 0.20) depending on the strontium doping content and heat treatment, *Ceram. Int.*, 2023, **49**, 10774.
25 Y. Xin, L. Shi, J. Zhao, X. Yuan, L. Hou and R. Tong, Electrical transport properties driven by magnetic competition in hole-doped perovskite $Pr_{1-x}Ba_xMnO_3$ ($0.25 \leq x \leq 0.36$), *Ceram. Int.*, 2021, **47**, 19464.
26 H. Rahmouni, A. Selmi, K. Khirouni and N. Kallel, Chromium effects on the transport properties in $La_{0.7}Sr_{0.3}Mn_{1-x}Cr_xO_3$, *J. Alloys Compd.*, 2012, **533**, 93.
27 R. Hanen, A. Mleiki, H. Rahmouni, N. Guermazi, K. Khirouni, E. K. Hlil and A. Cheikhrouhou, Effect of the nature of the dopant element on the physical properties of X-PrCaMnO system (X = Cd, Sr, and Pb), *J. Magn. Magn. Mater.*, 2020, **508**, 166810.
28 H. Baaziz, A. Tozri, E. Dhahri and E. K. Hlil, Effect of particle size reduction on the structural, magnetic properties and the spin excitations in ferromagnetic insulator $La_{0.9}Sr_{0.1}MnO_3$ nanoparticles, *Ceram. Int.*, 2015, **41**, 2955.
29 W. Hizi, M. Wali, H. Rahmouni, K. Khirouni and E. Dhahri, Examination of charge-carriers hopping and identification of relaxation phenomenon and blocking effect in perovskite system, *Eur. Phys. J. Plus*, 2024, **139**, 156.

30 R. Mendoza, J. Oliva, K. P. Padmasree, A. I. Mtz-Enriquez, A. Hayat and V. Rodriguez- Gonzalez, A sustainable avocado-peel based electrode for efficient graphene supercapacitors: enhancement of capacitance by using Sr doped $LaMnO_3$ perovskites, *Ceram. Int.*, 2022, **48**, 30967.

31 A. V. Pashchenko, N. A. Liedienov, I. V. Fesych, Q. Li, V. G. Pitsyuga, V. A. Turchenko, V. G. Pogrebnyak, B. Liu and G. G. Levchenko, Smart magnetic nanopowder based on the manganite perovskite for local hyperthermia, *RSC Adv.*, 2020, **10**, 30907.

32 W. Hizi, H. Rahmouni, K. Khirouni and E. Dhahri, Consistency between theoretical conduction models and experimental conductivity measurements of strontium-doped lanthanum manganite, *J. Alloys Compd.*, 2023, **957**, 170418.

33 Y. Regaieg, G. Delaizir, F. Herbst, L. Sicard, J. Monnier, D. Montero, B. Villeroy, S. Ammar-Merah, A. Cheikhrouhou, C. Godart and M. Koubaa, Rapid solid-state synthesis by spark plasma sintering and magnetic properties of $LaMnO_3$ perovskite manganite, *Mater. Lett.*, 2012, **80**, 195.

34 C. Zener, Interaction between the d-Shells in the Transition Metals. II. Ferromagnetic Compounds of Manganese with Perovskite Structure, *Phys. Rev.*, 1951, **82**, 403.

35 M. C. Dimri, H. Khanduri and R. Stern, Effects of aliovalent dopants in $LaMnO_3$: Magnetic, structural and transport properties, *J. Magn. Magn. Mater.*, 2021, **536**, 168111.

36 M. Arunachalam, P. Thamilmaran, S. Sankarrajan and K. Sakthipandi, Ultrasonic studies on sodium-doped $LaMnO_3$ perovskite material, *Cogent Phys.*, 2015, **2**, 1067344.

37 A. Tozri, E. Dhahri and E. K. Hlil, Impact of vacancy and Na substitutions on the critical magnetic behavior in polycrystalline $La_{0.8}Pb_{0.2}MnO_3$, *Phys. Lett. A*, 2011, **375**, 1528.

38 H. Liu, Y. Li, H. Zhang, Y. Chen, L. Chen, X. Dong and K. Chen, The role of disorder in sodium-doped $LaMnO_3$, *Phys. Status Solidi A*, 2011, **208**, 2373.

39 L. Malavasi, M. C. Mozzati, I. Alessandri, L. E. Depero, C. B. Azzoni and G. Flor, Sodium-doped $LaMnO_3$ thin films: Influence of substrate and thickness on physical properties, *J. Phys. Chem. B*, 2004, **108**, 13643.

40 S. Roy, Y. Q. Guo, S. Venkatesh and N. Ali, Interplay of structure and transport properties of sodium-doped lanthanum manganite, *J. Phys.: Condens. Matter*, 2001, **13**, 9547.

41 D. Varshney, D. Choudhary, M. W. Shaikh and E. Khan, Electrical resistivity behaviour of sodium substituted manganites: electron-phonon, electron-electron and electron-magnon interactions, *Eur. Phys. J. Plus B*, 2010, **76**, 327.

42 J. Vergara, R. J. Ortega-Hertogs and V. Madurga, Effect of disorder produced by cationic vacancies at the B sites on the electronic properties of mixed valence manganites, *Phys. Rev. B: Condens. Matter Mater. Phys.*, 1999, **60**, 1127.

43 M. Oumezzine, S. Kallel, O. Peña, N. Kallel, T. Guizouarn, F. Gouttefangeas and O. Mohamed, Correlation between structural, magnetic and electrical transport properties of barium vacancies in the $La_{0.67}Ba_{0.33-x}\square_xMnO_3$ (x = 0, 0.05, and 0.1) manganite, *J. Alloys Compd.*, 2014, **582**, 640.

44 B. Arun, V. R. Akshay, K. Devi Chandrasekhar, G. R. Mutta and M. Vasundhara, Comparison of structural, magnetic and electrical transport behavior in bulk and nanocrystalline Nd-lacunar $Nd_{0.67}Sr_{0.33}MnO_3$ manganites, *J. Magn. Magn. Mater.*, 2019, **472**, 74.

45 B. Sudakshina, K. K. Supin and M. Vasundhara, Effects of Nd-deficiency in $Nd_{0.67}Ba_{0.33}MnO_3$ manganites on structural, magnetic and electrical transport properties, *J. Magn. Magn. Mater.*, 2022, **542**, 168595.

46 B. Arun, V. R. Akshay and M. Vasundhara, Observation of enhanced magnetocaloric properties with A-site deficiency in $La_{0.67}Sr_{0.33}MnO_3$ manganite, *Dalton Trans.*, 2018, **47**, 15512.

47 J. Makni-Chakroun, R. M'nassri, W. Cheikhrouhou-Koubaa, M. Koubaa, N. Chniba-Boudjada and A. Cheikhrouhou, Effect of A-site deficiency on investigation of structural, magnetic and magnetocaloric behaviors for (LaSr)-lacunar manganites, *Chem. Phys. Lett.*, 2018, **707**, 61.

48 F. Elleuch, M. Triki, M. Bekri, E. Dhahri and E. K. Hlil, A-site-deficiency-dependent structural, magnetic and magnetoresistance properties in the $Pr_{0.6}Sr_{0.4}MnO_3$ manganites, *J. Alloys Compd.*, 2015, **620**, 249.

49 A. Bosak, C. Dubourdieu, M. Audier, J. P. Senateur and J. Pierre, Compositional effects on the structure and magnetotransport properties of lacunar $La_{1-x}MnO_{3-\delta}$ films ($x > 0$) grown by MOCVD, *Appl. Phys. A*, 2004, **79**, 1979.

50 M. Smari, I. Walha, E. Dhahri and E. K. Hlil, Structural, magnetic and magnetocaloric properties of Ag-doped $La_{0.5}Ca_{0.5-x}Ag_xMnO_3$ compounds with $0 \leq x \leq 0.4$, *J. Alloys Compd.*, 2013, **579**, 564.

51 R. M'nassri, W. Cheikhrouhou-Koubaa, N. Chniba Boudjada and A. Cheikhrouhou, Effect of barium-deficiency on the structural, magnetic, and magnetocaloric properties of $La_{0.6}Sr_{0.2}Ba_{0.2-x}\square_xMnO_3$ ($0 \leq x \leq 0.15$), *J. Appl. Phys.*, 2013, **113**, 073905.

52 R. A. Young, *The Rietveld Method*, Oxford University Press, New York, 1993.

53 B. Vertruyen, J.-F. Fagnard, Ph. Vanderbemden, M. Ausloos, A. Rulmont and R. Cloots, Electrical transport and magnetic properties of Mn_3O_4–$La_{0.7}Ca_{0.3}MnO_3$ ceramic composites prepared by a one-step spray-drying technique, *J. Eur. Ceram. Soc.*, 2007, **27**, 3923.

54 N. Mtiraoui, A. Dhahri, M. Oumezine, J. Dhahri and E. Dhahri, Effects of nonmagnetic silver Ag doping on the structural, magnetic and electric properties in $La_{0.67}Pb_{0.33}MnO_3$ manganese oxides, *J. Magn. Magn. Mater.*, 2011, **323**, 2831.

55 N. Dhahri, A. Dhahri, K. Cherif, J. Dhahri, H. Belmabrouk and E. Dhahri, Effect of Co substitution on magnetocaloric effect in $La_{0.67}Pb_{0.33}Mn_{1-x}Co_xO_3$ ($0.15 \leq x \leq 0.3$), *J. Alloys Compd.*, 2010, **507**, 405.

56 D. Shannon, Revised Effective Ionic Radii and Systematic Studies of Interatomic Distances in Halides and Chalcogenides, *Acta Crystallogr., Sect. A: Cryst. Phys., Diffr., Theor. Gen. Crystallogr.*, 1976, **32**, 751.

57 M. Khlifi, M. Bejar, O. EL Sadek, E. Dhahri, M. A. Ahmed and E. K. Hlil, Structural, magnetic and magnetocaloric properties of the lanthanum deficient in $La_{0.8}Ca_{0.2-x}\square_xMnO_3$ (x = 0–0.20) manganites oxides, *J. Alloys Compd.*, 2011, **509**, 7410.

58 R. Skini, M. Khlifi, E. Dhahri and E. K. Hlil, Lanthanum Deficiency Effect on the Structural, Magnetic and Transport Properties of the $La_{0.8-x}\square_xCa_{0.2}MnO_3$ Manganites Oxides, *J. Supercond. Novel Magn.*, 2014, **27**, 247.

59 M. Wali, R. Skini, M. Khlifi, E. Dhahri and E. K. Hlil, A giant magnetocaloric effect with a tunable temperature transition close to room temperature in Na-deficient $La_{0.8}Na_{0.2-x}\square_xMnO_3$ manganites, *Dalton Trans.*, 2015, **44**, 12796.

60 A. Hadded, J. Massoudi, S. Gharbi, E. Dhahri, A. Tozri and M. R. Berber, Study of physical properties of a ferromagnetic spinel $Cu_{1.5}Mn_{1.5}O_4$: spin dynamics, magnetocaloric effect and critical behavior, *RSC Adv.*, 2021, **11**, 25664.

61 S. Brion, F. Ciorcas, G. Chouteau, P. Lejay, P. Radaelli and C. Chaillout, Magnetic and electric properties of $La_{1-\delta}MnO_3$, *Phys. Rev. B: Condens. Matter Mater. Phys.*, 1999, **59**, 1304.

62 K. Funke, Jump relaxation in solid electrolytes, *Prog. Solid State Chem.*, 1993, **22**, 111.

63 G. E. Pike, AC Conductivity of scandium oxide and a new hopping model for conductivity, *Phys. Rev. B: Solid State*, 1972, **6**, 1572.

64 K. Maan Sangwan, N. Ahlawat, S. Rani, S. Rani and R. S. Kundu, Influence of Mn doping on electrical conductivity of lead free $BaZrTiO_3$ perovskite ceramic, *Ceram. Int.*, 2018, **44**, 10315.

65 A. S. Nowick and B. S. Lim, Analysis of ac conductivity data for $Na_2O_3SiO_2$ glass by stretched exponential and Jonscher power-law methods, *J. Non-Cryst. Solids*, 1994, **172**, 1389.

66 W. Hizi, M. Gassoumi, H. Rahmouni, A. Guesmi, N. B. Hamadi and E. Dhahri, Effect of Sintering Temperature and Polarization on the Dielectric and Electrical Properties of $La_{0.9}Sr_{0.1}MnO_3$ Manganite in Alternating Current, *Materials*, 2022, **15**, 3683.

67 S. R. Elliott, A theory of ac conduction in chalcogenide glasses, *Philos. Mag.*, 1977, **36**, 1291.

68 M. Coşkun, Ö. Polat, F. M. Coşkun, Z. Durmuş, M. Çağlar and A. Türüt, Frequency and temperature dependent electrical and dielectric properties of $LaCrO_3$ and Ir doped $LaCrO_3$ perovskite compounds, *J. Alloys Compd.*, 2018, **740**, 1012.

69 G. Nag Bhargavi, A. Khare, T. Badapanda, M. Shahid Anwar and N. Brahme, Electrical characterizations of $BaZr_{0.05}Ti_{0.95}O_3$ perovskite ceramic by impedance spectroscopy, electric modulus and conductivity, *J. Mater. Sci.: Mater. Electron.*, 2017, **28**, 16956.

70 Ch. Rayssi, S. El Kossi, J. Dhahri and K. Khirouni, Colossal dielectric constant and non-debye type relaxor in $Ca_{0.85}Er_{0.1}Ti_{1-x}Co_{4x/3}O_3$ (x = 0.15 and 0.2) ceramic, *J. Alloys Compd.*, 2018, **759**, 93.

71 P. Bruce, High and low frequency Jonscher behavior of an ionically conducting glass, *Solid State Ionics*, 1985, **15**, 247.

72 A. K. Jonscher, The universal dielectric response, *Nature*, 1977, **267**, 673.

73 A. K. Jonscher and M. S. Frost, Weakly frequency-dependent electrical conductivity in a chalcogenide glass, *Thin Solid Films*, 1976, **37**, 267.

74 L. Malavasi, M. C. Mozzati, C. B. Azzoni, G. Chiodelli and G. Flor, Role of oxygen content on the transport and magnetic properties of $La_{1-x}Ca_xMnO_{3+\delta}$ manganites, *Solid State Commun.*, 2002, **123**, 321.

75 W. Hizi, H. Rahmouni, N. E. Gorji, A. Guesmi, N. B. Hamadi, L. Khezami, E. Dhahri, K. Khirouni and M. Gassoumi, Impact of sintering temperature on the electrical properties of $La_{0.9}Sr_{0.1}MnO_3$ manganite, *Catalysts*, 2022, **12**, 340.

76 R. Charguia, S. Hcini, M. Boudard and A. Dhahri, Microstructural properties, conduction mechanism, dielectric behavior, impedance and electrical modulus of $La_{0.6}Sr_{0.2}Na_{0.2}MnO_3$ manganite, *J. Mater. Sci.: Mater. Electron.*, 2019, **30**, 2975.

77 H. Rahmouni, M. Nouiri, R. Jemai, N. Kallel, F. Rzigua, A. Selmi, K. Khirouni and S. Alaya, Electrical conductivity and complex impedance analysis of 20% Ti-doped $La_{0.7}Sr_{0.3}MnO_3$ perovskite, *J. Magn. Magn. Mater.*, 2007, **316**, 23.

78 H. Rahmouni, R. Jemai, M. Nouiri, N. Kallel, F. Rzigua, A. Selmi, K. Khirouni and S. Alaya, Admittance spectroscopy and complex impedance analysis of Ti-modified $La_{0.7}Sr_{0.3}MnO_3$, *J. Cryst. Growth*, 2008, **310**, 556.

79 K. Hayat, M. A. Rafiq, S. K. Durrani and M. M. Hasan, Impedance spectroscopy and investigation of conduction mechanism in $BaMnO_3$ nanorods, *Phys. B*, 2011, **406**, 309.

80 A. I. Tovstolytkin, A. N. Pogorily, V. V. Kotov, A. G. Belous and O. I. V'yunov, Effect of the crystal structure defectiveness on magnetic state of sodium-doped lanthanum manganites, *Funct. Mater.*, 2004, **11**, 721.